CrystEngComm

Accepted Manuscript

ROYAL SOCIETY OF CHEMISTRY

www.rsc.org/crystengcomm

CrystEngComm

RSCPublishing

ARTICLE

Ultra-rapid formation of ZnO hierarchical structures from dilution–induced supersaturated solutions†

Jing Wang, Sichao Hou, Lizhao Zhang, Jincai Chen and Lan Xiang*

Cite this: DOI: 10.1039/x0xx00000x

Received 00th January 2012,
Accepted 00th January 2012

DOI: 10.1039/x0xx00000x

www.rsc.org/

A facile additive-free solution method has been developed to fabricate ZnO star-like assemblies, nanosheet-based microspheres and nanorod-assemblies, by rapid dilution of zinc-bearing alkaline solution with water at 60 °C. The shape of the nanoscale building blocks in the hierarchical structures depends on the supersaturations, which can be adjusted by varying the dilution ratios or the ratios of $[OH^-]$ to $[Zn^{2+}]$. The experimental results indicate that with the increase of supersaturation, the building blocks of the hierarchical structures evolve from nanorods, nanosheets to nanoparticles. The formation of ZnO nanorod-assemblies involve the initial precipitation of ε-$Zn(OH)_2$ intermediate followed by a relative slow phase-transformation process, while ZnO nanosheet-based microspheres and star-like assemblies are constructed within 30 seconds owing to the rapid increase of supersaturation induced by dilution, involving the oriented attachment and the random aggregation mechanisms, respectively. Photoluminescence results reveal that the hierarchical structures are rich with singly and doubly ionized oxygen vacancies. The photocatalytic activities of the ZnO hierarchical structures were also evaluated by the degradation of rhodamine B under ultraviolet light. The photocatalytic performance depends on the content of oxygen vacancies as well as the specific surface area.

1. Introduction

Control over the shape and orientation of inorganic nanostructures has been a long-standing goal in revealing the relationship between crystal facets and their properties. Recently, significant efforts have been made to synthesize ZnO nanostructures, and growing attention has been paid to the self-assembly of low-dimensional ZnO nanoscale building blocks with controllable shape and orientation (nanoparticles, nanorods and nanosheets, *etc.*) into hierarchical structures, which demonstrate enhanced performances in functional devices as electronics, sensors, solar cells and photo-catalysis compared to mono-morphological structures.[1-4]

Solution-based strategies have been developed to synthesize ZnO hierarchical structures, including mainly the precursor-induced route, the sequential nucleation and growth route and the direct precipitation route, *etc.* The precursor-induced route involves the pre-synthesis of precursors with specific morphology (nest-like zinc hydroxide carbonate[5], flower-like basic zinc acetate[6], sheet-like zinc glycerol[7] and bi-pyramidal zinc glycolate[8], *etc.*) and their hydrothermal/thermal conversion to hierarchical structures. The sequential nucleation and growth route is based on the stepwise fabrication of the building blocks, including the formation of the primary structures and the subsequent nucleation and growth of the secondary or even the ternary structures on specific sites of previous structures.[9-12] Compared with the above two approaches in which multi-step procedures are needed, the direct precipitation route is more attractive since ZnO hierarchical structures can be fabricated simply by the one-pot solution process. Capping agents or surfactants were usually employed to direct the oriented growth and self-assembly of the nanoscale building blocks, based on the selective adsorption or complexing effects.[13-20] With the aim of avoiding the use of toxic reagents or expensive surfactants, some additive-free one-pot processes have been recently developed, and it was reported that the morphology of ZnO hierarchical structures was controlled by process parameters including the precursors type,[21, 22] solution composition,[23, 24] temperature[25] and reaction time[26], *etc.* Particularly, it has been widely demonstrated that the shape and orientation of the building blocks strongly depended on the precursor concentration, and possible mechanisms have been proposed.[21, 27, 28] Sun *et al.*[28] synthesized ZnO hierarchical structures in solution containing KOH and $Zn(NO_3)_2$ and attributed the evolution of the building blocks from nanosheets to nanoneedles to the enhancement of etching along [001] of

ZnO in concentrated KOH solution. Cho *et al.*[27] prepared ZnO hierarchical structures (assembled by nanosheets, nanoneedles, nanorods, and nanocones) from $Zn(CH_3COO)_2$-Na_2O_2 system and suggested that the morphology was connected with the concentration ratio of $Zn(OH)_4^{2-}$. Tong *et al.*[21] fabricated ZnO hierarchical nanostructures assembled by nanosheets, nanorods, and nanopetals at 120 °C by modulating the bases (NaOH, NH_3 and ethanediamine) and the molar ratios of the base to Zn^{2+}, proposing that the morphology of ZnO was connected with $[Zn(OH)_4^{2-}]$ as well as the nucleation and growth rates of ZnO. Moreover, the aggregation or oriented attachment mechanisms were usually proposed for the oriented growth and self-organization of the building blocks.[3, 13, 24, 28-30] Nevertheless, it is still desirable to gain further insight into the correlations among the synthetic condition, morphology evolution and corresponding mechanisms, so as to promote the systematic design and fabrication of ZnO hierarchical structures. Furthermore, it is also noticed that comparative long reaction time (typical 2~16 h) was usually needed for the construction of well-defined ZnO hierarchical structures in the previous works, it remains a challenge for the development of ultra-rapid synthesis strategy.

Some previous works demonstrated the shape and orientation of the ZnO nanostructures fabricated by solution methods were connected with the supersaturation. For example, Morin *et al.*[31] suggested that an extreme low supersaturation (precursor concentrations: 30 μM) favored the dislocation-driven oriented growth of ZnO along c-axis, forming ZnO nanowires and nanotubes with high aspect ratios. He *et al.*[32] demonstrated that a higher supersaturation favored the growth of ZnO on (100) planes. Zhang *et al.*[33] synthesized the flower- and rod-like ZnO nanostructures by tuning the ratios of NaOH to $Zn(CH_3COO)_2$ and suggested that the shape of ZnO nanostructures depended on the solution supersaturation. Besides, some other works revealed that the growth of ZnO nanostructures could be accelerated by increasing the supersaturation. For example, He *et al.* and Shi *et al.* reported that with the assistant of ultrasonic, ZnO hollow spheres assembled by nanoparticles[34] and ZnO microspheres assembled by nanosheets[35] were formed within 1 h and 15 min, respectively, the rapid nucleation and growth of ZnO were attributed to the high local supersaturation created by the ultrasonic. However, up to now to the best of our knowledge, little work concerned the role of supersaturation in controlling the shape of the nanoscale building blocks, and the ultra-rapid formation of ZnO hierarchical structures within 1 minute has not been reported yet.

Herein, a facile additive-free solution approach has been developed to synthesize ZnO hierarchical structures assembled by tunable building blocks from dilution-induced supersaturated solutions. The correlation between supersaturation and morphology was established, and related mechanisms were proposed for the ultra-rapid formation of ZnO hierarchical structures within 30 seconds. In addition, the photoluminescence properties and photocatalytic activities of the ZnO hierarchical structures were also investigated. The supersaturation-driven route may be also helpful for the oriented growth and self-assembly of other inorganic nanostructures.

2. Experimental

2.1 Synthesis

Fig. 1 Schematic illustration for preparation of ZnO hierarchical structures.

Commercial chemicals with analytical grade were used without further purification and deionized water with a resistivity > 18 $M\Omega \cdot cm^{-1}$ was used in the experiments. The morphology and particle size distribution of the commercial ZnO powders are shown in Fig. S1†. The commercial ZnO powders are composed of irregular particles with diameters of 20-1000 nm, and most of the particles fall into the size range of 100 to 300 nm.

Fig. 1 shows the typical process for the preparation of ZnO hierarchical structures from the supersaturated zinc-bearing alkaline solutions, using commercial ZnO powders and NaOH as the raw materials. ZnO (4.07~23.25 g) and NaOH (40.00 g) were dissolved into water (100.0 mL) at room temperature to form a transparent solution ($[Zn^{2+}]$=0.50~2.86 $mol \cdot L^{-1}$, $[OH^-]$=10.00 $mol \cdot L^{-1}$, $[OH^-]/[Zn^{2+}]$=20:1~3.5:1). 3.0 mL of the above solution was then diluted with certain amount of water quickly at 60 °C to form a supersaturated system (note: water should be pre-heated to 60 °C). The supersaturation was adjusted via two approaches: (i) fixing $[OH^-]/[Zn^{2+}]$=6.78:1 and varying the dilution ratio (α) in the range of 5~200 (α was defined as the ratio of the solution volume after dilution to the solution volume before dilution); (ii) keeping α=50 and varying $[OH^-]/[Zn^{2+}]$ in the range of 20:1~3.5:1 by adjusting the amount of ZnO in the zinc-bearing alkaline solution. After ageing the supersaturated solution at 60 °C for 0~2.0 h, the precipitates were collected, washed with deionized water and dried in a vacuum oven at 25 °C for 24 h.

2.2 Analysis and characterization

To determine the concentrations of the soluble zinc, the suspensions were centrifuged (5000 rpm) and the top clear solutions were neutralized with 1:1 (v) hydrochloric acid, then buffered to pH=10 with NH_4OH-NH_4Cl solution and titrated by EDTA method.

The composition and structure of the samples were identified by an X-ray powder diffractometer (XRD, Bruker-AXS D8 Advance, Germany) using CuKα (λ=0.154178 nm) radiation. The morphology and microstructures of the samples were examined with a field emission scanning electron microscopy (FESEM, JSM 7401F, JEOL, Japan) and a high resolution transmission electron microscopy (HRTEM, JEM-2010, JEOL,

Japan), respectively. The Brunauer Emmett Teller (BET) specific surface areas of the products were analyzed by the nitrogen adsorption analyzer (Quadrasorb-S1; Quantachrome, USA). The room temperature photoluminescence spectra were measured on a Hitachi F-7000 luminescence spectrometer using a Xe lamp with an excitation wavelength of 325 nm.

2.3 Photocatalytic measurements

The photocatalytic activities were evaluated at 25 ^{o}C by the degradation of rhodamine B (RhB) under ultraviolet light irradiation from two UV lamps (Philips, 8 W). 0.01 g ZnO sample was dispersed in 100 mL of RhB aqueous solution (4 mg·L^{-1}). Before irradiating, the above suspension was stirred in the dark for 30 min to achieve the adsorption-desorption equilibrium. The suspension was sampled at an interval of 20 min and centrifuged to remove the catalysts at 8000 rpm for 10 min. The UV-vis absorption spectra of the centrifuged solutions were measured by an Agilent UV-8453 spectrophotometer to determine the concentration of RhB.

3. Results and discussion

The degree of supersaturation undergoes a sudden increase when the unsaturated zinc-bearing alkaline solution is diluted with water owing to the variation of solubility, since ZnO is amphoteric and have lower solubility in lower concentration NaOH solution. Here, supersaturation (S) is defined as S= $\ln(c_i/c_0)$, where c_i and c_0 are the initial concentration and equilibrium concentration of the system, respectively.[36] To convert c to S, the equilibrium concentration (c_0) was empirically determined by analyzing the final soluble zinc concentration of the growth solution after prolonging the reaction time to 10 h when the concentration was quite stable. Fig. 2 shows the variations of $\ln c_i$, $\ln c_0$ and S with the dilution ratio (α), the vertical distance between curve a and curve b reflects the corresponding S after dilution (Fig. 2c). The supersaturations at α=5, 10, 25, 50 and 200 were 0.42, 0.95, 1.26, 2.34 and 3.51, respectively. These results indicated that S could be well-adjusted by simply varying the dilution ratio.

It was observed experimentally that the solutions became cloudy immediately after dilution if S ≥ 1.26, while the induction time for precipitation was prolonged to several minutes if S ≤ 0.95. Fig. 3 shows the XRD patterns of the samples formed at different S and reaction time. In the case of S=1.26, orthorhombic ε-$Zn(OH)_2$ (JCPDS 38–0385) formed at 30 s (Fig. 3a), similarly, the precipitates formed at low supersaturation (S=0.42 and 0.95) after reaction for 10 min were also identified as pure ε-$Zn(OH)_2$. Otherwise, prolonging the ageing time to 2 h at 60 ^{o}C led to the complete conversion from ε-$Zn(OH)_2$ to würtzite ZnO (JCPDS card 36-1451) (Fig. 3b). Würtzite ZnO formed directly at 30 s in the case of S=2.34 and 3.51 (Fig. 3c and d). These results revealed that high supersaturation (S ≥ 2.34) favored the ultra-rapid nucleation and growth of ZnO, while ZnO formed slowly at low supersaturation (S ≤ 1.26), involving the pre-formation of ε-$Zn(OH)_2$ intermediate and its subsequent conversion to ZnO.

The variation in structural characteristics of the as-prepare ZnO samples could be also obtained from the XRD patterns. The broadening and decreasing in intensity of the diffraction peaks from Fig. 2b to d indicated the decrease of the crystallite size and the crystallization of ZnO, and it was also observed that the increase of S from 1.26, 2.34 to 3.51 led to the decrease of the intensity ratio of (100) to (002) diffraction peaks ($I_{(100)}/I_{(002)}$) from 1.46, 0.97 to 0.75, respectively, implying that high supersaturation would inhibit the oriented growth of ZnO along c-axis.

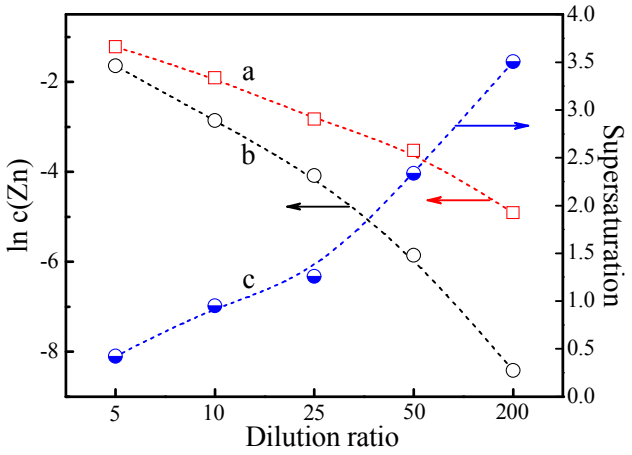

Fig. 2 Variations of $\ln c_i$ (a), $\ln c_0$ (b) and S (c) with dilution ratio.

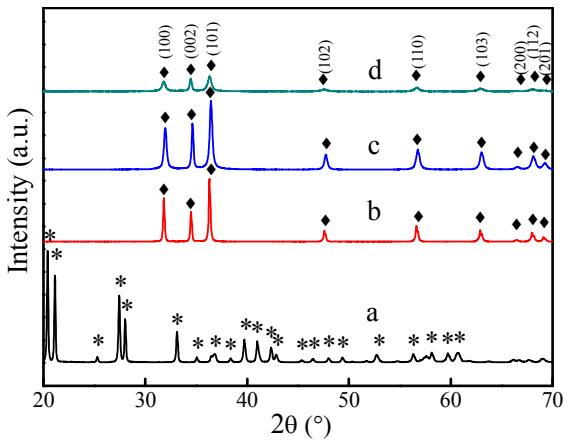

Fig. 3 XRD patterns of samples formed at different S and reaction time. S: (a, b) 1.26, (c) 2.34, (d) 3.51; time: (a, c, d) 30 s, (b) 2.0 h; *: ε-$Zn(OH)_2$, ◆: ZnO.

Fig. 4 shows the SEM images of the samples formed at different S and reaction time. ε-$Zn(OH)_2$ micro-octahedrons formed at S=1.26 after 30 s of reaction (Fig. 4a) and converted to ZnO assemblies composed of radial-aligned nanorods at 2.0 h (Fig. 4b). ZnO microspheres with a diameter of 3-8 μm assembled by nanosheets were produced at S=2.34 (Fig. 4c and 4d). The nanosheets (thickness: 40~80 nm) were intersected with each other and decorated with nanorod-arrays (diameters: 20~40 nm, average length: ~50 nm), different from those microspheres assembled by smooth nanosheets in the former works.[15, 17, 28] Star-like ZnO assemblies with a diameter of 1~5

μm composed of petals projected radially from one center were fabricated at S=3.51 (Fig. 4e and f). The petals were assembled by paralleled nanorods (diameter: 10~20 nm, inserted TEM image in Fig. 4f), and the surface of the star-like ZnO was not smooth but covered by nanoparticles, such a novel structure has not been reported previously. To sum up, the nanoscale building blocks of the ZnO hierarchical structures formed at S=1.26, 2.34 and 3.51 were nanorods, nanosheets and nanoparticles, respectively.

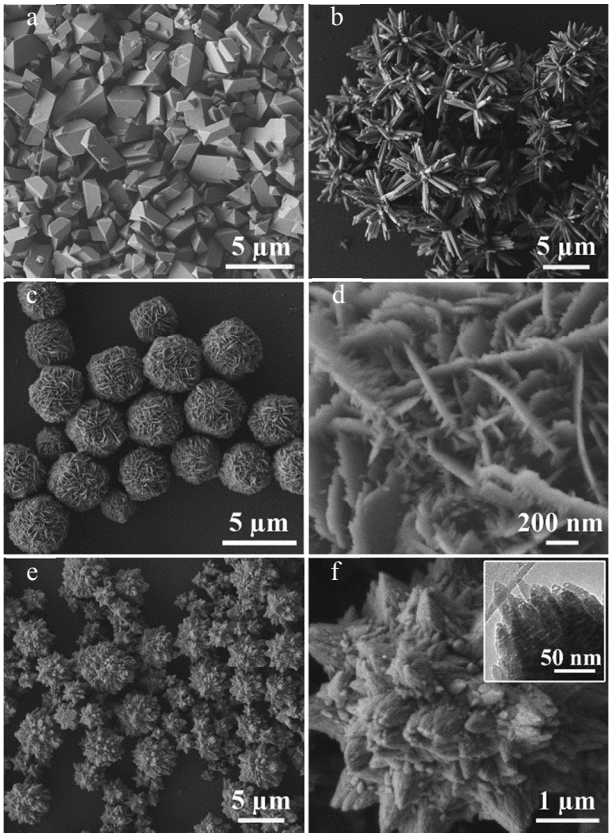

Fig. 4 SEM images of samples formed at different S and reaction time. S: (a, b) 1.26, (c, d) 2.34, (e, f) 3.51; time: (a, c-f) 30 s, (b) 2.0 h. The inset in Fig. 4f is a TEM image of a petal from the star-like architectures.

Another complication arises in interpreting the supersaturation driven shape evolution of the building blocks, that is, tuning the supersaturation by adjusting dilution ratio would also change the OH^- concentration, which was previously considered as a decisive factor in ZnO growth. [18, 22, 27] To eliminate the effect of $[OH^-]$ on the growth, S was adjusted by tuning the ratios of $[OH^-]/[Zn^{2+}]$ in the range of 3.5:1-20:1 while keeping α at 50 and the initial $[OH^-]$ at 0.2 $mol \cdot L^{-1}$. The variation of S with $[OH^-]/[Zn^{2+}]$ is shown in Fig. 5. The increase of $[OH^-]/[Zn^{2+}]$ from 3.5:1 to 20:1 led to the decrease of S from 3.0 to 1.25. Three regions are indexed according to the morphology evolution (The corresponding SEM images of the ZnO hierarchical structures formed at different S adjusted by $[OH^-]/[Zn^{2+}]$ are shown in Fig. 6): formation of ZnO star-like assemblies at $S \geq 3.00$ (region I, Fig. 6a), nanosheet-based microspheres at $1.95 \leq S \leq 2.64$ (region II, Fig. 6b-d), and formation of ε-$Zn(OH)_2$ which subsequent converted to ZnO nanorod-assemblies at $S \leq 1.54$ (region III). Products with mixed morphologies were obtained if S was adjusted in the intervals of these regions (Fig. S2†). For example, hierarchical structures assembled by both nanoparticles and nanosheets were obtained at S=2.86 (Fig. S2a†), while in the sample formed at S=1.77, both nanosheet-based microspheres and nanorod-assemblies were observed (Fig. S2b†). It was also observed the decrease of S in the range of 2.64 to 1.95 led to the formation of nanosheets decorated with denser and longer nanorods (Fig. 4d and Fig. 6b-d). The above results indicated that the increase of S led to the gradual evolution of the nanoscale building blocks in the ZnO hierarchical structures from nanorods to nanosheets, and finally to nanoparticles, no matter the supersaturation was adjusted by α or $[OH^-]/[Zn^{2+}]$.

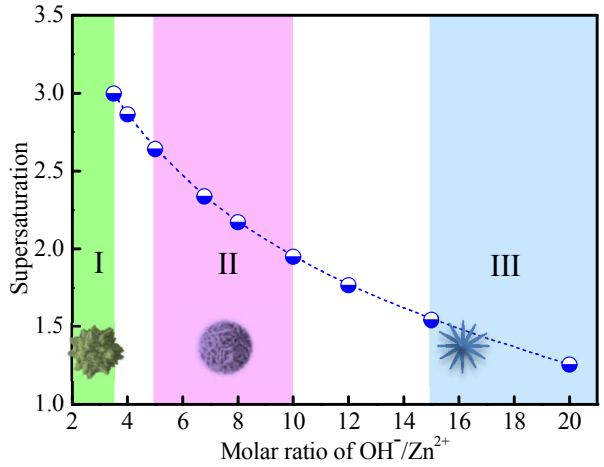

Fig. 5 Variation of S with $[OH^-]/[Zn^{2+}]$ (α=50). Three regions were indexed by colors according to the morphology evolution. Region: (I) S ≥3.00; (II) 1.95≤S≤2.64, (III) S≤1.54. Insets are the corresponding schematic illustration of the products.

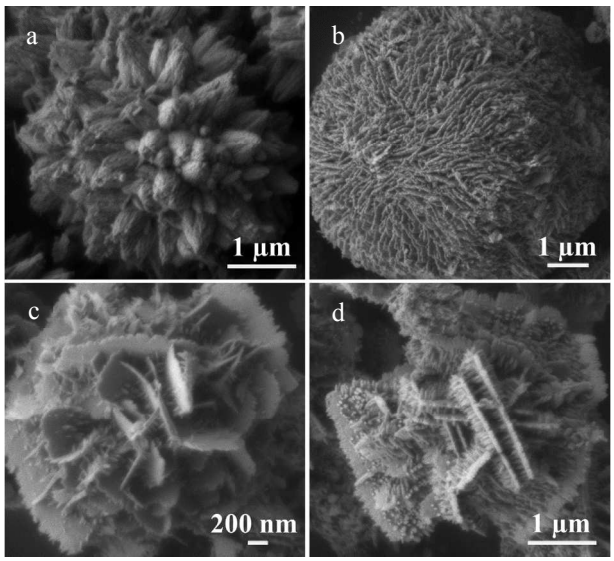

Fig. 6 SEM images of the samples formed at different S tuned by $[OH^-]/[Zn^{2+}]$. $[OH^-]/[Zn^{2+}]$: (a) 3.5 (S=3.00); (b) 5 (S=2.64); (c) 8 (S=2.17); (d) 10 (S=1.95).

The shape evolution of the nanoscale building block of the hierarchical structures was usually attributed to the variation of growth rate of different crystal orientation with the solution composition.[21, 27, 37] However, in the current study, strong dependence of the formation mechanism on the supersaturation was demonstrated. At low supersaturations, the formation of ZnO nanorod-assemblies was intermediated by ε-$Zn(OH)_2$ phase. Time-resolved investigation of the growth process of ZnO nanorod-assemblies at S=1.26 was performed, the morphology and phase characterization of the intermediate products (Fig. S3†) revealed the growth occurred via a phase-transformation process, which involved both the dissolution-precipitation and in-situ crystallization mechanisms, consisting with the previous observations.[38-40] Hence, the following part of this paper focuses on the mechanisms for the ultra-rapid formation of ZnO nanosheet-based microspheres and star-like assemblies at high supersaturations. Though nanocrystal-mediated self-assembly mechanisms have been proposed previously,[13, 15, 35] however, to date, the variation of the self-assemble behavior of nanocrystals with supersaturation has rarely been considered. Herein, two different self-assemble behaviors of nanocrystals including oriented attachment and random aggregation were observed at different supersaturations.

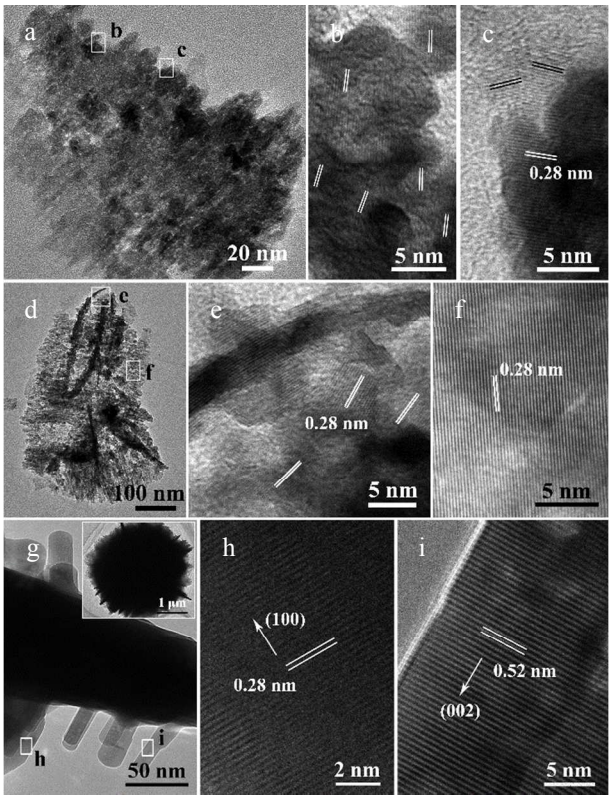

Fig. 7 TEM and HRTEM images of samples formed at S=2.34. Reaction time (s): (a-c) 0, (d-f) 10, (g-i) 30.

Fig. 7 shows the TEM and HRTEM images of the samples formed at different reaction time at S=2.34, keeping α=50 and $[OH^-]/[Zn^{2+}]$=6.78:1. Coarse nanosheets with poor crystallization formed immediately after dilution (Fig. 7a). The nanosheets were composed of self-organized adjacent particles sharing a similar crystallographic orientation (Fig. 7b, the spacings were 0.28 nm for all the measured lattice fringes, which were consistent with the interplanar spacings of $(01\bar{1}0)$ plane of hexagonal würtzite ZnO). Fig. 7c shows the attachment of two quasi-spherical particles to the edge of a nanosheet with a small misorientation. The above observations demonstrated the oriented attachment of ZnO nanocrystals at the initial formation stage of the ZnO nanosheets. The driving forces to assemble nanocrystals into nanosheets were generally attributed to anisotropic hydrophobic attraction and electrostatic interactions derived from dipole moments or surface charges.[41, 42] In the present case, hydrophobic attraction could be ruled out since no organic template/surfactant was added. Consider the anisotropic würtzite structure of ZnO, different surface charge distributions on different planes may favor the oriented attachment. The nanosheets were subsequently reconstructed in which the boundaries of the nanocrystal were eliminated and the polycrystalline nanosheets were fused into monocrystalline with smooth surfaces. For example, in the case of the nanosheet formed at 10 s, some areas were monocrystalline (Fig. 7f) while nanocrystal boundaries still remained in other areas (Fig. 7e). The nanosheets tended to assemble with each other to form microspheres to minimize the surface energies (Fig. 7d). The HRTEM images shown in Fig. 7b, c, e indicated that the oriented attachments were not strictly confined by crystal orientations but characterized by a misorientation at the interfaces. The dislocations originated from the imperfect oriented attachment may act as the "active sites" for the secondary nucleation and growth of the nanorods, leading to the formation of the nanorod-arrays on the nanosheets at 30 s (Fig. 7g), similar "imperfect oriented attachment" was observed by Penn *et al.* in the hydrothermal coarsening of titania nanocrystallines[43] and later was used to explain the defects-induced formation of complex polymorphic structures.[44, 45] The HRTEM image of the nanosheet in Fig. 7h exhibits well-resolved lattice fringes with a spacing of 0.28 nm, and lattice fringes with a spacing of 0.26 nm were also observed in other nanosheets, demonstrating the preferential growth of the nanosheets along (0001) and $(01\bar{1}0)$ directions with $\{2\bar{1}\bar{1}0\}$ planes as the exposed surfaces. Fig. 7i shows the HRTEM image of the nanorod grown on the nanosheet surface. The lattice fringes (0.52 nm) of the nanorod was consistent with the spacing of (002) plane of ZnO, revealing the oriented growth of the nanorod along c-axis.

Fig. 8 shows the TEM and HRTEM images of the samples formed at different reaction time, keeping S=3.51 (α=200 and $[OH^-]/[Zn^{2+}]$=6.78:1). ZnO nanospheres with a diameter of 10-100 nm formed immediately after dilution (Fig. 8a). The nanospheres were assembled randomly by nanocrystals with different orientations (Fig. 8b), and the inserted SAED pattern confirmed the polycrystalline nature of the nanospheres. The entropy-driven random aggregation should be response for the assembly of the nanocrystals.[46] The nanospheres may attach with each other or serve as cores for the subsequent attachment

of the nanoparticles which may further develop into nanorods, finally forming the star-like structures with petals (Fig. 8c) which were decorated with randomly assembled nanoparticles at 10 s (inset in Fig. 8c and Fig. 8d). The TEM and HRTEM image in Fig. 8e and f revealed that the petals were assembled by the paralleled nanorods showing a preferential growth along c-axis.

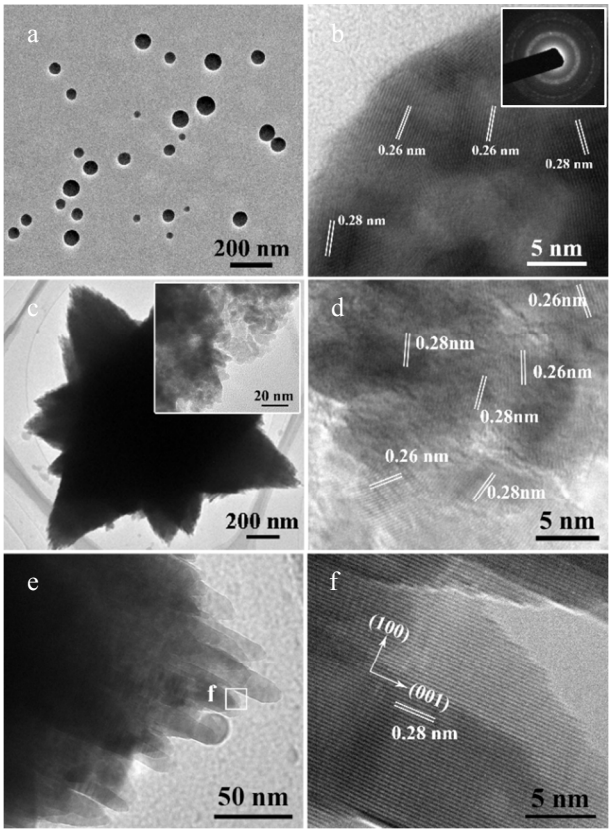

Fig. 8 TEM and HRTEM images of samples formed at S=3.51. Time(s): (a, b) 0, (c-f) 10. Inset in Fig. 8b is a SEAD pattern of the nanospheres.

On the basis of the above discussion, the schematic illustration of the formation mechanisms of ZnO hierarchical structures is shown in Fig. 9. The supersaturation of the zinc-bearing alkaline solution, which was adjusted by varying the dilution ratio or $[OH^-]/[Zn^{2+}]$, increased rapidly after the dilution. ε-$Zn(OH)_2$ formed at low supersaturation (S≤1.54) and subsequently converted to ZnO nanorod-assemblies via the phase transformation process. A higher supersaturation (1.95 ≤ S ≤2.64) promoted the direct nucleation of ZnO nanocrystals and their quick self-organization to the nanosheets and microspheres via oriented attachment. The decrease of S in the range of 2.64 to 1.95 promoted the secondary growth of nanorods on the surfaces of the nanosheets, which was driven by the dislocations originated from the imperfect oriented attachment. The further increase of the supersaturation (S≥3.00) led to the immediate assembly of the ZnO nanocrystals into nanospheres via random aggregation, the subsequent attachment and oriented growth of the nanoparticles on the nanospheres led to the final formation of star-like structures with petals composed of paralleled nanorods. Well-defined ZnO nanosheet-based microspheres and star-like assemblies could be constructed within 30 s at S≥1.95. In addition, it was notable that during the formation of nanosheet-based microspheres and star-like assemblies, the supersaturation decreased continuously due to the consumption of soluble zinc, leading to the oriented growth of nanorods in the hierarchical structures at the final stage.

To demonstrate the structure-induced enhancement of the photocatalytic performance of the hierarchical ZnO structures, the degradation of RhB was used to assess the photocatalytic activities of the samples obtained at S=1.26, 2.34 and 3.51. Fig. 10a shows absorption spectra of an aqueous solution of RhB (initial concentration: 4 mg/L, 100 mL) in the presence of 10 mg of the ZnO nanosheet-based microspheres under exposure to the ultraviolet light lamp for various durations, and the inset is the corresponding photographs of the RhB solutions. The absorption peak corresponding to RhB at 554 nm diminishes sharply and disappears completely after irradiation for about 160 min. Fig. 10b shows the curves of the concentration of RhB with UV light irradiation time over the commercial ZnO powders, nanorod-assemblies (NR), nanosheet-based microspheres (NS) and star-like assemblies (NP). Without any catalyst, only a slow decrease in the concentration of RhB was detected under UV irradiation. The specific surface areas of the star-like assemblies, nanosheets-based microspheres, nanorod-assemblies and commercial ZnO powders were evaluated to be 9.80, 18.00, 7.01 and 10.34 m^2/g, respectively. However, all the synthesized samples showed enhanced photocatalytic activities compared to commercial ZnO powders and the activity increased in turn for: nanorod- assemblies, star-like assemblies and nanosheets-based microspheres. Hence, it was believed that the photocatalytic activity not only related to the specific surface area, but also the type and concentration of defects in the samples.

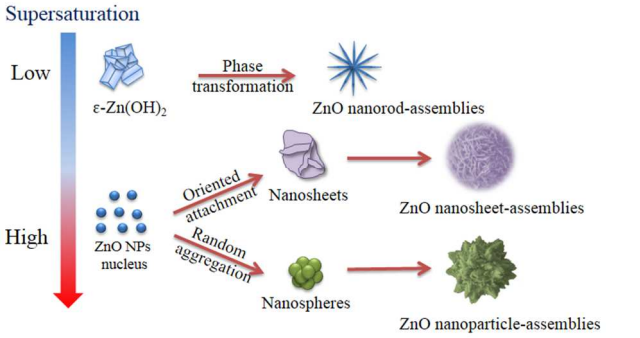

Fig. 9 Schematic illustration for formation mechanisms of ZnO hierarchical structures.

The room temperature photoluminescence (PL) spectra were recorded to get the information about the defect states of the samples, as shown in Fig. 11. The commercial ZnO powders displayed an ultraviolet (UV) emission peak with maximal intensity at around 384 nm, which was due to the excitonic recombination of the photo-generated holes in the valence band

(VB) and the electrons in the conduction band (CB).[47] However, the characteristic UV emission was not present in the as-prepared three samples, indicating that high concentration of defects were introduced into the hierarchical structures. In the visible region, a broad and weak blue-green emission centered at about 495 nm was observed for commercial ZnO powders, which could be divided into the blue emission at ~480 nm originated from the zinc vacancies (V_{Zn}), and the yellow one at ~520 nm which was commonly attributed to the singly charged oxygen vacancies (V_O^+).[48] However, the hierarchical structures exhibited broad-band green-yellow emissions centered at 555 nm, which could be divided into two peaks, including the green emission at ~520 nm originated from V_O^+, and the yellow one at ~580 nm originated from doubly charged oxygen vacancies (V_O^{++}).[49] The PL results demonstrated that the defects type evolved from coexisting V_{Zn} and V_O^+ in the commercial ZnO powders to coexisting V_O^+ and V_O^{++} in the hierarchical structures, and the content of V_O^{++} increased in turn for: commercial ZnO powders, nanorod-assemblies, nanosheet-based microspheres and star-like assemblies, indicating that V_O^{++} may play an important role in enhancing the photocatalytic performance.

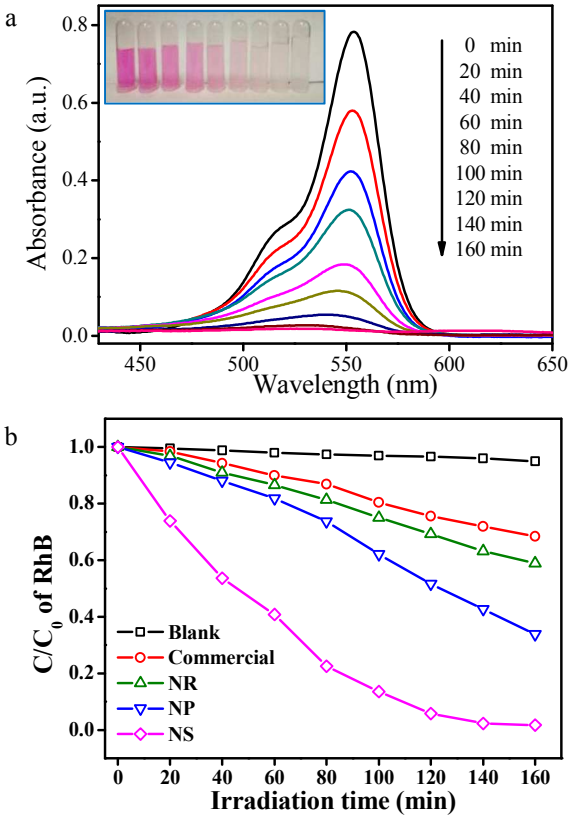

Fig. 10 (a) Adsorption changes of RhB aqueous solution in the presence of ZnO nanosheet-based microspheres, inset: corresponding photographs of the RhB solutions; (b) the photocatalytic degradation of RhB under UV light irradiation in the presence different ZnO samples.

The photocatalytic degradation of organic dye occurs by an indirect pathway involving hydroxyl radicals as the oxidizing intermediate as follows:[50]

$$ZnO + hv \rightarrow ZnO(e_{CB}^- + h_{VB}^+) \quad (1)$$

$$h_{VB}^+ + H_2O \rightarrow H^+ + {}^{\bullet}OH \quad (2)$$

$$dye + {}^{\bullet}OH \rightarrow oxidized\ products \quad (3)$$

When ZnO is irradiated by UV light with a photon energy hv that matches or exceeds the bandgap energy (E_g) of ZnO, conduction band electrons (e_{CB}^-) and valence band holes (h_{VB}^+) are generated on the surface of ZnO (eqn 1). h_{VB}^+ can react with water adhering to the surfaces of ZnO to form hydroxyl radicals (•OH) which can result in the oxidation of organic dye (eqn 2 and 3). According to previous studies,[51] the role of V_O^{++} in the photocatalytic reaction process can be described by eqn 4 and 5, and the schematic illustration of the band structure and photocatalytic mechanism of ZnO with the existence of V_O^{++} is shown as inset in Fig. 11.

$$V_O^{++} + e_{CB}^- \rightarrow V_O^+ \quad (4)$$

$$V_O^+ + O_2 \rightarrow V_O^{++} + {}^{\bullet}O_2^- \quad (5)$$

The V_O^{++} defects can be considered to be the active sites of the ZnO catalyst, which work as electron acceptors and can trap the photogenerated electrons temporarily to reduce the undesirable surface recombination of electrons and holes (eqn 4), leading to an increase in the photocatalytic efficiency. It was demonstrated that the hierarchical structures possessed higher content of V_O^{++} compared to commercial ZnO powders, which may enhance the photocatalytic activity. Therefore, we proposed that the photocatalytic activities of the samples depended on the content of V_O^{++} as well as the specific surface area.

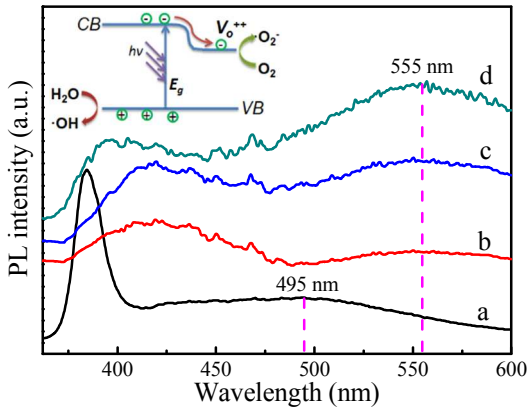

Fig. 11 Room-temperature photoluminescence spectra of the ZnO samples: (a) commercial ZnO powders; (b) nanorod-assemblies; (c) nanosheet-based microspheres; (d) star-like assemblies. Inset: schematic illustration of the band structure and photocatalytic mechanism of ZnO with the existence of V_O^{++}.

Conclusions

ZnO hierarchical structures with tunable morphology were synthesized from the dilution-induced supersaturated solutions. The supersaturation (S) was adjusted in the range of 1.26 to 3.51 by varying the dilution ratio or $[OH^-]/[Zn^{2+}]$. The nanoscale building blocks of the hierarchical structures evolved from nanorods ($S \leq 1.54$), nanosheets ($1.95 \leq S \leq 2.64$) to

nanoparticles (S≥3.00). ZnO nanosheet-based microspheres and star-like assemblies were constructed within 30 s, involving the oriented attachment and the random aggregation mechanisms, respectively. Photocatalytic measurements demonstrated the ZnO nanosheet-based microspheres exhibited highest photo-degradation activity. The enhanced photocatalytic performance was linked with combined effects of specific surface area and content of V_O^{++}.

Acknowledgements

This work was supported by the National Science Foundation of China (No. 51174125 and No. 51234003), National Hi-Tech Research and Development Program of China (863 Program, 2012AA061602) and National Key Technology Research and Development Program of China (2013BAC14B02).

Notes and references

** Department of Chemical Engineering, Tsinghua University, Beijing, 10084, China. Fax: +86-10-62772051; Tel: +86-10-62788984; E-mail: xianglan@mail.tsinghua.edu.cn*

†Electronic Supplementary Information (ESI) available: characterization of the commercial ZnO powders, additional SEM images and XRD patterns of the as-synthesized products and intermediates. See DOI: 10.1039/b000000x/

1. M. Ahmad, S. Yingying, A. Nisar, H. Sun, W. Shen, M. Wei and J. Zhu, *Journal of Materials Chemistry*, 2011, **21**, 7723-7729.
2. Z. Jing and J. Zhan, *Advanced Materials*, 2008, **20**, 4547-4551.
3. Q. Zhang, T. P. Chou, B. Russo, S. A. Jenekhe and G. Cao, *Angewandte Chemie*, 2008, **120**, 2436-2440.
4. Q. Wu, X. Chen, P. Zhang, Y. Han, X. Chen, Y. Yan and S. Li, *Crystal Growth and Design*, 2008, **8**, 3010-3018.
5. X. Wang, W. Liu, J. Liu, F. Wang, J. Kong, S. Qiu, C. He and L. Luan, *ACS Applied Materials & Interfaces*, 2012, **4**, 817-825.
6. J. Zhan, H. Dong, Y. Liu, Y. Wang, Z. Chen and L. Zhang, *CrystEngComm*, 2013, **15**, 10272-10277.
7. Y. Hong, C. Tian, B. Jiang, A. Wu, Q. Zhang, G. Tian and H. Fu, *J. Mater. Chem. A*, 2013, **1**, 5700-5708.
8. J. Das, I. R. Evans and D. Khushalani, *Inorganic chemistry*, 2009, **48**, 3508-3510.
9. V.-M. Guérin and T. Pauporté, *Energy & Environmental Science*, 2011, **4**, 2971-2979.
10. J. Qiu, M. Guo and X. Wang, *ACS Applied Materials & Interfaces*, 2011, **3**, 2358-2367.
11. T. L. Sounart, J. Liu, J. A. Voigt, M. Huo, E. D. Spoerke and B. McKenzie, *Journal of the American Chemical Society*, 2007, **129**, 15786-15793.
12. T. Zhang, W. Dong, M. Keeter-Brewer, S. Konar, R. N. Njabon and Z. R. Tian, *Journal of the American Chemical Society*, 2006, **128**, 10960-10968.
13. H. Lu, S. Wang, L. Zhao, J. Li, B. Dong and Z. Xu, *Journal of Materials Chemistry*, 2011, **21**, 4228-4234.
14. M. Raula, M. H. Rashid, T. K. Paira, E. Dinda and T. K. Mandal, *Langmuir*, 2010, **26**, 8769-8782.
15. Y. Sun, L. Wang, X. Yu and K. Chen, *CrystEngComm*, 2012, **14**, 3199-3204.
16. A.-J. Wang, Q.-C. Liao, J.-J. Feng, P.-P. Zhang, A.-Q. Li and J.-J. Wang, *CrystEngComm*, 2012, **14**, 256-263.
17. M. Wang, Y. Zhang, Y. Zhou, F. Yang, E. J. Kim, S. H. Hahn and S. G. Seong, *CrystEngComm*, 2013, **15**, 754-763.
18. P. Hu, N. Han, X. Zhang, M. Yao, Y. Cao, A. Zuo, G. Yang and F. Yuan, *Journal of Materials Chemistry*, 2011, **21**, 14277-14284.
19. Y. Sun, R. Zou, W. Li, Q. Tian, J. Wu, Z. Chen and J. Hu, *CrystEngComm*, 2011, **13**, 6107-6113.
20. U. Maiti, K. Chattopadhyay, S. Karan and B. Mallik, *Scripta Materialia*, 2010, **62**, 305-308.
21. G.-X. Tong, F.-F. Du, Y. Liang, Q. Hu, R.-N. Wu, J.-G. Guan and X. Hu, *Journal of Materials Chemistry B*, 2013, **1**, 454-463.
22. U. N. Maiti, S. Maiti and K. K. Chattopadhyay, *CrystEngComm*, 2012, **14**, 640-647.
23. P. Hu, X. Zhang, N. Han, W. Xiang, Y. Cao and F. Yuan, *Crystal Growth & Design*, 2011, **11**, 1520-1526.
24. T. Zhai, S. Xie, Y. Zhao, X. Sun, X. Lu, M. Yu, M. Xu, F. Xiao and Y. Tong, *CrystEngComm*, 2012, **14**, 1850-1855.
25. D. Wu, Z. Gao, F. Xu, Z. Shi, W. Tao and K. Jiang, *CrystEngComm*, 2012, **14**, 7934-7941.
26. Q.-P. Luo, B.-X. Lei, X.-Y. Yu, D.-B. Kuang and C.-Y. Su, *Journal of Materials Chemistry*, 2011, **21**, 8709-8714.
27. S. Cho, J.-W. Jang, J. S. Lee and K.-H. Lee, *Langmuir*, 2010, **26**, 14255-14262.
28. H. Sun, Y. Yu, J. Luo, M. Ahmad and J. Zhu, *CrystEngComm*, 2012, **14**, 8626-8632.
29. J.-J. Feng, Q.-C. Liao, A.-J. Wang and J.-R. Chen, *CrystEngComm*, 2011, **13**, 4202-4210.
30. D.-F. Zhang, L.-D. Sun, J. Zhang, Z.-G. Yan and C.-H. Yan, *Crystal Growth and Design*, 2008, **8**, 3609-3615.
31. S. A. Morin, M. J. Bierman, J. Tong and S. Jin, *Science*, 2010, **328**, 476-480.
32. Y. He, T. Yanagida, K. Nagashima, F. Zhuge, G. Meng, B. Xu, A. Klamchuen, S. Rahong, M. Kanai and X. Li, *The Journal of Physical Chemistry C*, 2013, **117**, 1197-1203.
33. Y. Zhang and J. Mu, *Nanotechnology*, 2007, **18**, 075606.
34. C. X. He, B. X. Lei, Y. F. Wang, C. Y. Su, Y. P. Fang and D. B. Kuang, *Chemistry-A European Journal*, 2010, **16**, 8757-8761.
35. Y. Shi, C. Zhu, L. Wang, C. Zhao, W. Li, K. K. Fung, T. Ma, A. Hagfeldt and N. Wang, *Chemistry of Materials*, 2013, **25**, 1000-1012.
36. I. V. Markov and I. V. Markov, *Crystal growth for beginners: fundamentals of nucleation, crystal growth and epitaxy*, World Scientific Singapore, 2003.
37. S. Singh, K. Barick and D. Bahadur, *CrystEngComm*, 2013, **15**, 4631-4639.
38. P. Li, H. Liu, B. Lu and Y. Wei, *The Journal of Physical Chemistry C*, 2010, **114**, 21132-21137.
39. M. Wang, Y. Zhou, Y. Zhang, S. H. Hahn and E. J. Kim, *CrystEngComm*, 2011, **13**, 6024-6026.
40. N. J. Nicholas, G. V. Franks and W. A. Ducker, *CrystEngComm*, 2012, **14**, 1232-1240.
41. Z. Tang, Z. Zhang, Y. Wang, S. C. Glotzer and N. A. Kotov, *Science*, 2006, **314**, 274-278.
42. Z. Zhang, Z. Tang, N. A. Kotov and S. C. Glotzer, *Nano letters*, 2007, **7**, 1670-1675.

43. R. L. Penn and J. F. Banfield, *Science*, 1998, **281**, 969-971.
44. M. Tsai, S. Chen and P. Shen, *Nano Letters*, 2004, **4**, 1197-1201.
45. Q. Lu, H. Zeng, Z. Wang, X. Cao and L. Zhang, *Nanotechnology*, 2006, **17**, 2098.
46. Z. Zhang, H. Sun, X. Shao, D. Li, H. Yu and M. Han, *Advanced Materials*, 2005, **17**, 42-47.
47. Y. Chen, D. Bagnall, H.-j. Koh, K.-t. Park, K. Hiraga, Z. Zhu and T. Yao, *Journal of Applied Physics*, 1998, **84**, 3912-3918.
48. H. Zeng, G. Duan, Y. Li, S. Yang, X. Xu and W. Cai, *Advanced Functional Materials*, 2010, **20**, 561-572.
49. K. Vanheusden, C. Seager, W. t. Warren, D. Tallant and J. Voigt, *Applied Physics Letters*, 1996, **68**, 403-405.
50. M. R. Hoffmann, S. T. Martin, W. Choi and D. W. Bahnemann, *Chemical reviews*, 1995, **95**, 69-96.
51. Y. Zheng, C. Chen, Y. Zhan, X. Lin, Q. Zheng, K. Wei, J. Zhu and Y. Zhu, *Inorganic chemistry*, 2007, **46**, 6675-6682.

Table of contents entry

Table of Contents Graphic

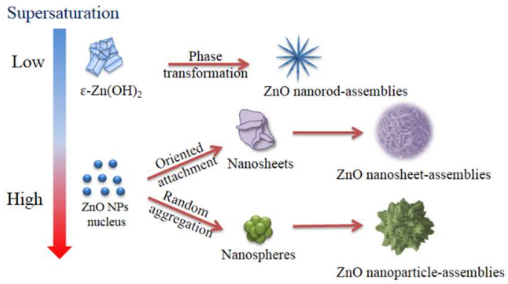

Textual abstract

ZnO hierarchical structures assembled by tunable nanoscale building blocks as nanorods, nanosheets and nanoparticles were synthesized from dilution-induced supersaturated solutions.